A 2-D Mesh-based Magnetic Equivalent Circuit Model for Hybrid Exciting Magnetic Lead Screw

Lixun Zhu, Junfei Wu, Ting Xu, Min Huang, Ning Gao, Kangan Wang, Wei Li, *Member*, *IEEE*,
Runhua Fan, Chang-seop Koh, *Senior Member*, *IEEE* and Frede Blaabjerg, *Fellow*, *IEEE*

Abstract—To reduce the computational time involved in analyzing the dynamic performance and conducting optimal design of a hybrid excitation magnetic lead screw (HEMLS)，a two-dimensional (2-D) mesh-based (MB) magnetic equivalent circuit (MEC) model is proposed. In the proposed model, the mesh structure does not need to be reconstructed at every time step; only the parameters of each element need to be updated to reflect the current status of the HEMLS. To simplify the proposed mesh-based MEC model, PM, and current exciting sources in one pole are considered as one magnetomotive force. In addition, the mesh density can be adjusted according to the solution region to reduce the computational cost. Finally, the proposed MB-MEC model is verified by comparing it with the static thrust force from the finite element method and prototype test under load and no-load conditions.

Index Terms—magnetic lead screw, magnetic equivalent circuit, wave energy conversion.

I. INTRODUCTION

In recent years, magnetic lead screw (MLS), as shown in Fig. 1, has attracted considerable attention in linear-rotational conversion applications due to the characteristics of high energy conversion efficiency, low friction, high operational reliability, and low maintenance cost. Typical applications include automobile transmission, medical devices, aerospace systems, and wave energy conversion [1]-[4]. The MLS can convert low-speed linear motion into high-speed rotational motion and vice versa by utilizing the spiral magnetic field coupling in the air gap between the mover and the rotor.

Several MLS topologies have been proposed, including traditional permanent magnet (PM) MLS, single spiral MLS, and current-excited MLS. However, the PM consumption is enormous for the traditional PM MLS because only helical PM exiting source exists on both rotor and mover [5]-[7]. The single spiral MLS has been proposed in [8]-[9] to reduce permanent magnet consumption by installing only one permanent magnet pole on the mover. However, the maximum thrust was still

reduced by half. Additionally, both the traditional PM MLS and the single spiral MLS exhibit poor dynamic performance due to the inability to adjust the magnetic field in the air gap. To improve the dynamic performance of the PM MLS, a current-excited MLS has been proposed in [10]-[11]. However, its maximum thrust force falls short of meeting specific requirements, such as those needed for wave energy conversion systems. Consequently, a hybrid excitation MLS (HEMLS) topology is proposed to provide both improved controllability in application and sufficiently high thrust forces to ensure the converter capacity [12].

The maximum thrust force is the most critical performance parameter used to determine the load capability. Therefore, a fast and accurate analysis method can help accelerate the optimal design process of the MLS.

So far, a variety of methods have been developed for modeling electric machines, such as numerical methods [12]-[17], Fourier models [18]-[20], and the magnetic equivalent circuit (MEC) models [21]-[24]. The numerical model is the most accurate one, but the calculation consumption is enormous, especially for the helical shape structure of the HEMLS. Even if the Fourier model can obtain satisfactory results, the reality model should be simplified; it is difficult to apply to the optimization process. The MEC model, for its ability to rapidly deliver accurate results without simplifying the motor topology, has gained significant attention in accelerating the design process of PM motors.

Generally, lumped parameter MEC models are mostly selected to analyze the characteristics of PM machines, and the results can match that of finite element analysis (FEA) [25]. Magnetic circuit analysis is based on the qualitative theoretical analysis [26], and it excels in analyzing the steady-state magnetic field and determining the maximum value of flux density [27]. However, for the transient magnetic field, the MEC models for every transient time should be developed to obtain dynamic magnetic field distribution. This means that

Lixun Zhu, Junfei Wu, Ting Xu, Min Huang, Ning Gao and Kangan Wang are with the Department of Electrical Engineering, Shanghai Maritime University, Shanghai 201306, China (e-mail: lixzhu@shmtu.edu.cn; 202230210087@stu.shmtu.edu.cn; ting.x@wustl.edu; minhuang@shmtu.edu.cn; ngao@shmtu.edu.cn; kawang@shmtu.edu.cn).

Wei Li is with the Department of Electrical Engineering, Tongji University, Shanghai, 201804, China (e-mail: liweimail@tongji.edu.cn).

Runhua Fan is with the College of Ocean Science and Engineering, Shanghai Maritime University, Shanghai 201306, China (e-mail: rhfan@shmtu.edu.cn)

Chang-seop Koh is with the Department of Electrical Engineering, Chungbuk National University, Choungju 21366, Korea (e-mail: kohcs@cbnu.ac.kr).

Frede Blaabjerg is with the Department of Energy Engineering, Aalborg University, Aalborg 9100, Denmark (e-mail: fbl@et.aau.dk).

> 2024-SECSC-1317 <

huge repetitive modeling work is often required in the process of optimal design for designers [28].

As the topology becomes more and more complex, traditional magnetic equivalent methods have been developed to address the limitations of magnetic circuit analysis. Tailored to specific modeling considerations, the MEC method develops two types of modeling approaches: the branch-based [29] and the mesh-based MEC [30]. The branch-based MEC, commencing with the practical flux path, represents a dynamic expansion and enhancement of magnetic circuit analysis. In contrast, the mesh-based MEC, built on a predefined mesh structure, simplifies the transition from distributed parameter methods to magnetic circuit analysis.

Although the above MEC methods have been applied to various types of motors, their application to MLS has been rarely studied. In this paper, a simplified two-dimensional (2-D) mesh-based MEC model is developed to analyze the performance of the HEMLS. Unlike conventional approaches, the mesh structure of the proposed model does not require reconstruction for each time instant; instead, only the parameter values of each element need to be updated to reflect the HEMLS's status.

To further simplify the proposed mesh-based MEC model, both PM and current exciting sources in one pole are considered as one magnetomotive force. Additionally, the mesh density can be adjusted based on the solution region to decrease he computational time. In the second section of this paper, the topology and principle of the proposed HEMLS are introduced. The theoretical basis and implementation details of the proposed MB-MEC model, including iterative methods will be presented in Section III with the numerical solutions . The effectiveness of the proposed methods is validated through comparisons with FEA and experimental results in Section IV and Section V, respectively. Finally, the conclusions are summarized in Section VI.

II. TOPOLOGICAL AND OPERATING PRINCIPLE OF HEMLS

A. Topological

The three-dimensional (3-D) diagram of the HEMLS topology, along with its 2-D top view and axial cross-sectional view, is shown in Fig. 4. As depicted, the HEMLS consists of two main parts: the mover and rotor. The rotor comprises the rotor core and its PM poles. The opposite spiral-shape PM poles are mounted on the inner surface of the rotor core alternatingly, as same with the traditional MLS, as shown in Fig. 4. The mover consists of the mover core, a spiral-shaped permanent magnet, and two-phase spiral-shaped windings. The spiral-shaped windings are fixed in the spiral-shape slots, which are grooved on the outer surface of the mover. As shown in Fig. 4(a), the alternating spiral-shaped PM poles are mounted on the surface of the spiral-shaped pole-shoe. To ensure proper functioning, the spiral direction of the PM and windings must align with the direction of the PM on the rotor.
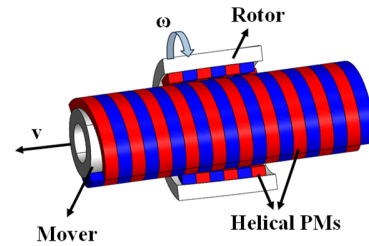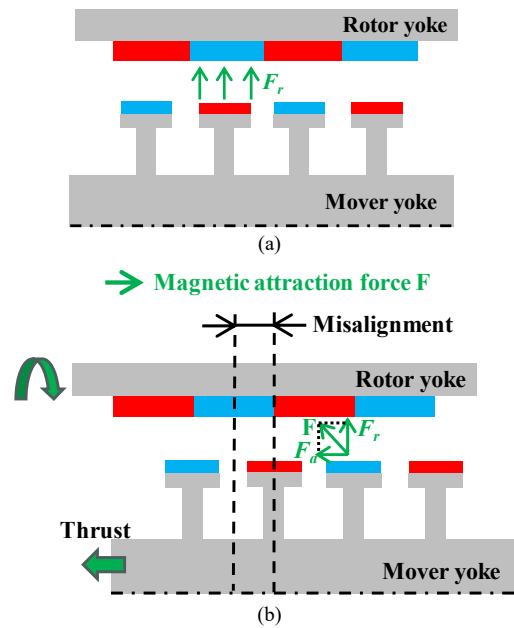

Fig. 1 Structure of MLS.

Fig. 2 The principle of the thrust or torque generation. (a) Magnetic stability position. (b) Magnetic attractive force due to the misalignment.
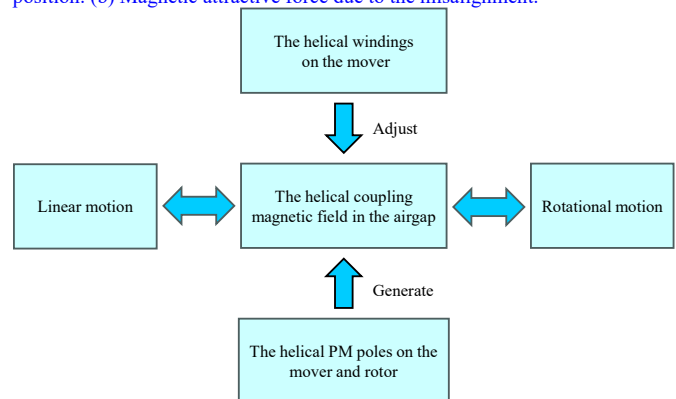

Fig. 3 The flow chart of the linear and rotational motion conversion principle.
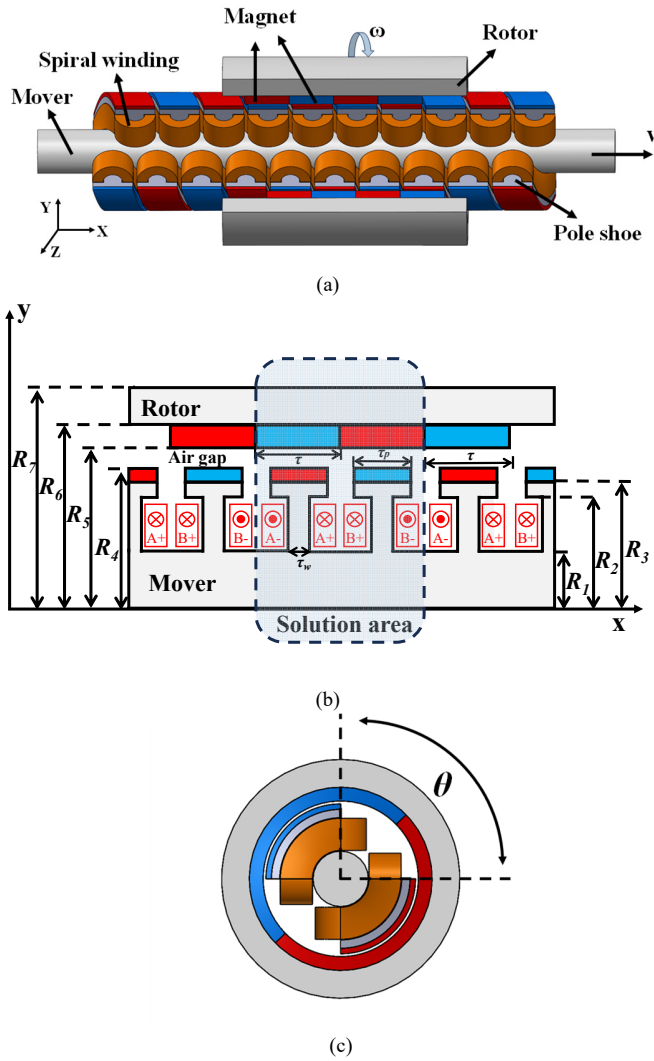
> 2024-SECSC-1317 <

(a)

(b)

(c)

Fig.4 Structure of the HEMLS. (a) 3-D structure. (b) 2-D axial cross-section (c) The top view.

(a)

(b)

Fig. 5 The main magnetic flux path of the HEMLS. (a) Initial position. (b) move half the pole pitch position.
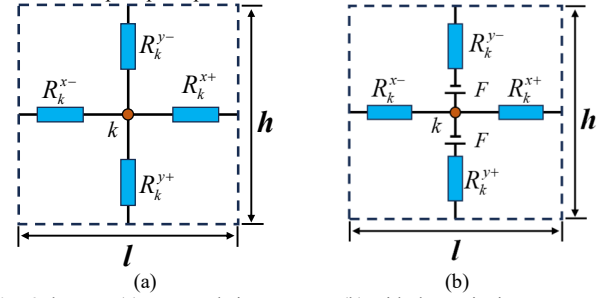
Fig. 6 element. (a) Core and air-gap parts. (b) with the excitation part.

B. Working principle

When the poles of the mover and the rotor are directly aligned in opposite positions, only a radial electromagnetic force f_r is present, and neither torque nor thrust will be generated. In this state, the magnetic screw is in a stable, as shown in Fig. 2(a). However, when a misalignment occurs between the poles of the mover and the rotor, as shown in Fig. 2(b), an axial electromagnetic force f_a is generated from the total magnetic attention force F at this position. This electromagnetic force f_a produces rotor torque or mover thrust due to the coupling effect of the helical-shape magnetic field in the air gap. Therefore, once the mover is driven back and forth along the x-axis by thrust, a misalignment between the pole of the rotor and the mover arises, enabling the rotor to rotate due to the resulting torque simultaneously. In addition, the helical magnetic field generated by the exciting windings on the mover can be controlled by adjusting the exciting current of the winding. A flowchart illustrating the principle of linear-rotational motion conversion is presented in Fig. 3.

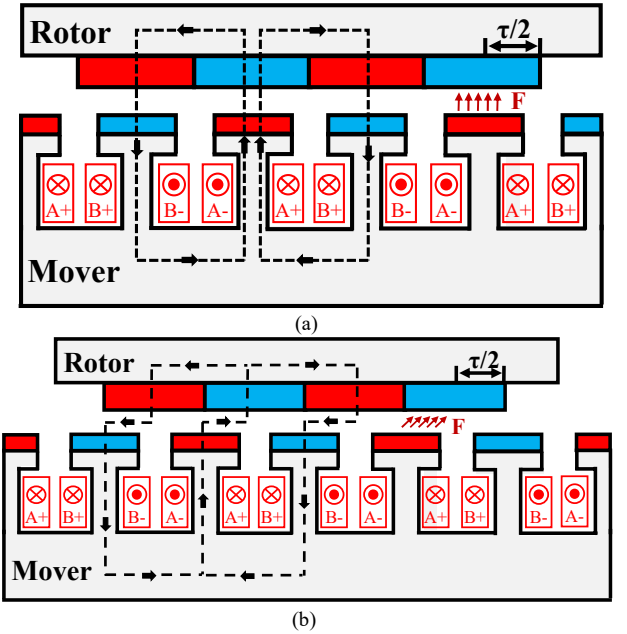When the mover moves a lead (λ) along the x-axis, the rotor

also rotates a circle of 2π rad along with the mover. According to the energy conservation law, if neglecting losses, the proposed HEMLS can convert a low-speed linear motion of the mover at a velocity of v into a high-speed rotational motion of the rotor at an angular velocity of ω, as described by the equation below:

$$F_t / T_r = \omega / v = 2\pi / \lambda \quad (1)$$

where F_t represents the axial thrust on the actuator, T_r denotes the torque of the rotor, and λ is the lead defined as $\lambda = 2p\tau$, where p represents the number of poles, and τ represents the pole pitch.

The main magnetic flux path of the HEMLS at different relative positions between the mover and rotor is illustrated in Fig. 5. When the relative position fixed at the relative position between the mover and the rotor is shown in Fig. 5(a), the thrust force of the mover $F_t = 0$ N, as there is no axial component of magnetic flux density (B). The maximum thrust force F_t can be achieved when the relative position between the mover and the rotor is fixed, as shown in Fig. 5(b). By applying a suitable current on the two-phase windings, the magnetic field can be either enhanced or reduced to meet various control requirements.

III. The proposed Mesh-Based MEC Model Of The HEMLS and Its Analysis

A. Solution region

According to the small spiral inclination structure of the HEMLS, a 2-D static magnetic field based on the cross-sectional view can be applied to evaluate its magnetic field distribution and performance. Accordingly, the region shown in Fig. 4(b) can be selected as the periodical region, reflecting the periodical cross-sectional structure of the HEMLS along the x-axis if the ending effect is neglected.
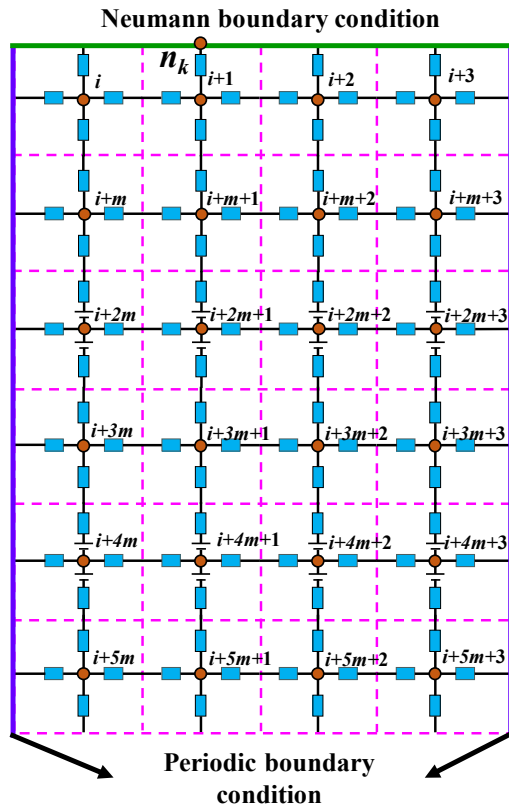

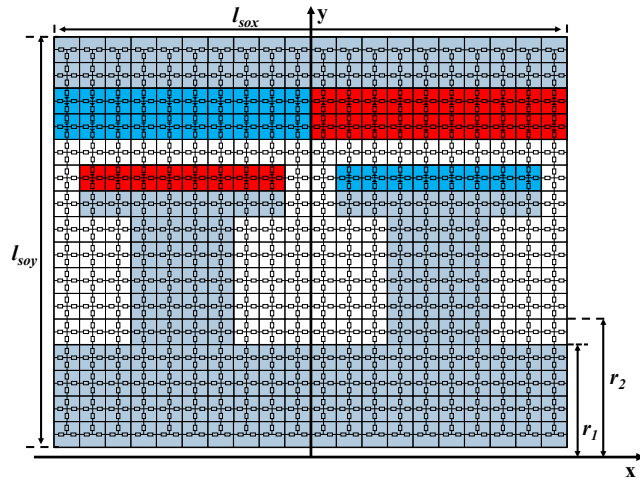**Fig. 7.** Example of the elements arrangement with the boundary condition

Fig. 8. the whole proposed mesh-based MEC model

B. Magnetic circuit element

In the proposed MB-MEC model, the solution region can be discretized using rectangular mesh elements, as shown in Fig. 4(b). While the meshing can be non-uniform in both the x-direction and y-direction, all elements are designed to have equal width in both the x-direction and y-direction. This uniformity simplifies the implementation process, particularly for dynamic modeling. Therefore, uniform square mech elements will be used for the solution region. During the meshing process, each material boundary must align precisely with the edges of the MB, ensuring each material contains only one element.

Each element consists of a potential node with its four reluctances along the four directions around the potential node, as shown in Fig. 6. If there is excitation in the element, the excitation can be present as a magnetomotive force (MMF) connected in series with the corresponding reluctance, as shown in Fig. 6(b). In Fig. 7, the pink dotted-line squares are used to mark each element. As illustrated, the symbols "+" and "-" are used to distinguish the reluctances on both sides of the potential node number k along one direction. For instance, R_k^{x-} and R_k^{x+} represent the reluctance on the left and right sides of the potential
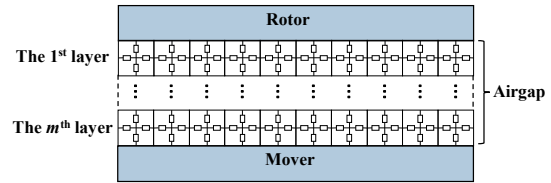

Fig. 9 The mesh distribution in the airgap
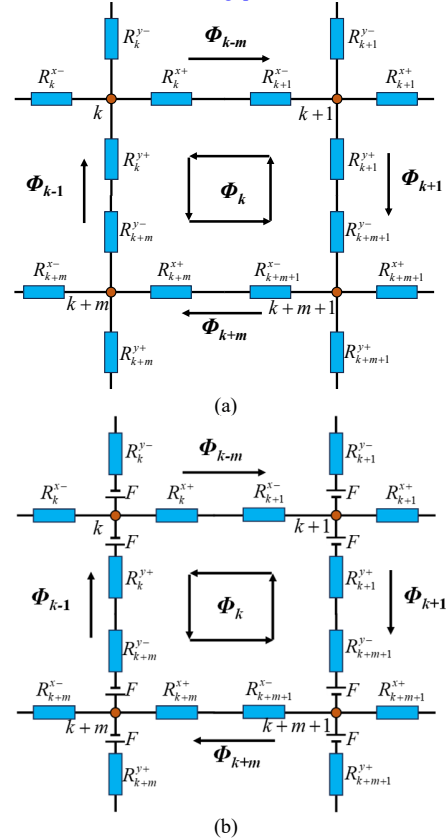

(a)

(b)

Fig. 10 example of the mesh. (a) without MMF. (b) containing MMF

> 2024-SECSC-1317 <

node number k along the x-direction, respectively. Similarly, R_k^{y-} and R_k^{y+} represent the reluctances of the bottom and top sides of the potential node number k along the y-direction, respectively. Each reluctance is defined as

$$R_k^{x+} = R_k^{x-} = \frac{l}{2\mu_0\mu_k S_{yz}} \quad (2)$$

$$R_k^{y+} = R_k^{y-} = \frac{h}{2\mu_0\mu_k S_{xz}} \quad (3)$$

where l represents the width of the mesh element, h represents the height of the mesh element, μ_k is the relative permeability of the corresponding number k mesh element, and μ_0 is the vacuum permeability. S_{yz} and S_{xz} refers to the cross-sectional areas of the element k in the yz and xz planes, respectively.

The number of layers in each solution region, including airgap, mover, and rotor, can be adjusted to increase the accuracy of the calculation results. The mesh distribution within the airgap region is illustrated in Fig. 9.

C. Exciting source

In the HEMLS, both PM and winding with applied current are modeled as exciting sources. The equivalent MMF of PM (F_{pm}) can be expressed as:

$$F_{pm} = \frac{B_r h_m}{2\mu_0\mu_{pm}} \quad (4)$$

where B_r is the remanence of PM, μ_{pm} is the relative permeability of PM, and h_m is the height of the PM segment.

In this paper, the MMF can be directly superimposed into the mover permanent magnet mesh element. The direction of the MMF can be determined based on the flowing direction of the current following the right-hand spiral criterion. The MMF generated by the energized winding can be calculated by the following formula:

$$F_c = \int_l H \cdot dl = N_c i_k \quad (5)$$

where F_c is the MMF generated by the excited coil, H is the magnetic field strength, N_c is the number of winding coils, and i_k is the magnitude of the injected current.

D. The proposed mesh-based MEC modeling

After discretizing, the whole proposed mesh-based MEC model can be established through interconnected neighboring elements. An example of the elements' arrangement with boundary conditions is shown in Fig. 7. In this figure, the model is defined by the Neumann boundary condition and the periodic
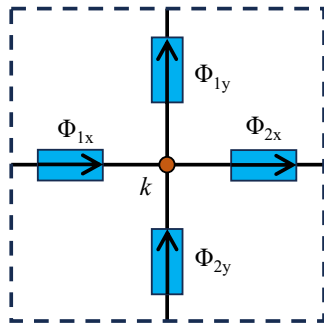
boundary condition.

Fig. 8 illustrates the complete proposed mesh-based MEC model.

As shown in Fig. 7, every four adjacent nodes form a square-shaped mesh, and the mesh number is the same as the number of the top left node. For a single mesh, as depicted in Fig. 10, the mesh current analysis method from circuit analysis can be applied. The following balanced equation or a mesh without MMF, as shown in Fig. 10(a), can be derived:

$$R_{(k,k)}\Phi_k + R_{(k,k-m)}\Phi_{k-m} + R_{(k,k-1)}\Phi_{k-1} + R_{(k,k+m)}\Phi_{k+m} + R_{(k,k+1)}\Phi_{k+1} = 0 \quad (6)$$

The balanced equation for a mesh containing MMF, as shown in Fig. 10(b), is:
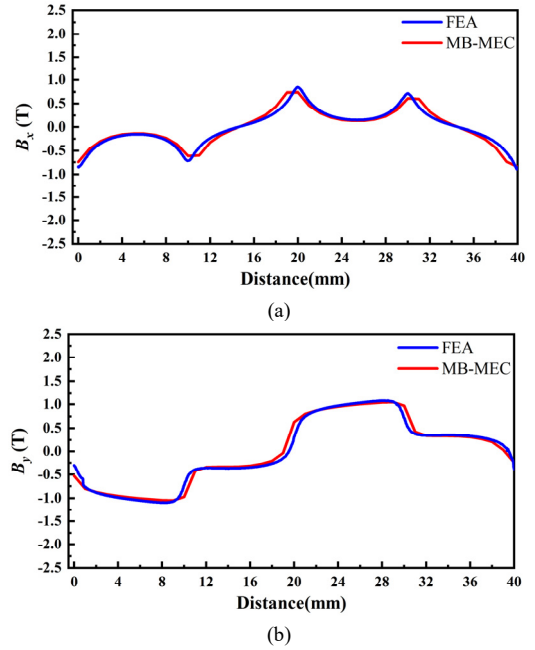

Fig. 12 The flux density distribution in air gap under no-load condition. (a) B_x. (b) B_y.
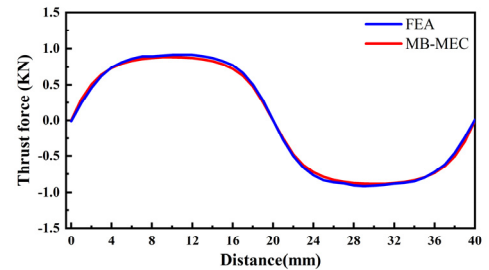

Fig. 13 The comparison results of thrust force under no-load condition.

Fig. 11. Flux direction of elements.

TABLE I
SPECIFICATION OF THE HEMLS

Symbol	Parameters	Values
R_1	Rod radius	10 (mm)
R_2	High moving teeth	22 (mm)
R_3	T tooth outer diameter	25 (mm)
R_4	Mover outside diameter	27 (mm)
R_5	Inner diameter of rotor	28 (mm)
R_6	Outer diameter of rotor PM	33 (mm)
R_7	Outer diameter of rotor	43 (mm)
τ	Rotor PM width	20 (mm)
τ_p	Mover PM width	18 (mm)
τ_w	Mover tooth width	12 (mm)
B_r	Magnet remanence	1.2 (T)
μ_0	Vacuum permeability	$4\pi \times 10^{-7}$ (N·A^{-2})
θ	Interval angle	90°
l	Coupling length	40 (mm)
n_c	Number of windings	45
n_{pm}	Number of turns of rotor PM	2

$$R_{(k,k)}\Phi_k + R_{(k,k-m)}\Phi_{k-m} + R_{(k,k-1)}\Phi_{k-1} + R_{(k,k+m)}\Phi_{k+m} + R_{(k,k+1)}\Phi_{k+1} = 4F_{pm} \quad (7)$$

$$R_{(k,k)} = R_k^{x+} + R_{k+1}^{x-} + R_k^{y-} + R_{k+m}^{y+} + R_{k+m}^{x+} + R_{k+m+1}^{x-} + R_{k+1}^{y-} + R_{k+m+1}^{y+} \quad (8)$$

$$R_{(k,k-m)} = -\left(R_k^{x+} + R_{k+1}^{x-}\right) \quad (9)$$

$$R_{(k,k-1)} = -\left(R_k^{y-} + R_{k+m}^{y+}\right) \quad (10)$$

$$R_{(k,k+m)} = -\left(R_{k+m}^{x+} + R_{k+m+1}^{x-}\right) \quad (11)$$

$$R_{(k,k+1)} = -\left(R_{k+1}^{y-} + R_{k+m+1}^{y+}\right) \quad (12)$$

By considering each mesh, the flux in each branch can be obtained by solving the following equations:

$$\begin{pmatrix} R(1,1) & R(1,2) & \cdots & R(1,n) \\ R(2,1) & R(2,2) & \cdots & R(2,n) \\ \vdots & \vdots & \ddots & \vdots \\ R(n,1) & R(n,2) & \cdots & R(n,n) \end{pmatrix} \begin{bmatrix} \Phi(1) \\ \Phi(2) \\ \vdots \\ \Phi(n) \end{bmatrix} = \begin{bmatrix} F(1) \\ F(2) \\ \vdots \\ F(n) \end{bmatrix} \quad (13)$$

where $F(i)$ represents the MMF contained in the ith mesh, $R(i,i)$ denotes the reluctance value contained in the ith mesh, $R(i,j)$ denotes the reluctance value between the ith mesh and the jth mesh, and n represents the total amount of mesh.

Among them, the reluctance matrix $[R]$ has the following characteristics:

$$\begin{cases} R(i,i) \geq 0, R(i,j) \leq 0 & i \neq j \\ R(i,i) = -\sum_{j=1, j\neq i}^{n} R(i,j) & N_{sx} < i < n - N_{sx} \\ R(i,j) = R(j,i) & i \neq j \end{cases} \quad (14)$$

Where N_{sx} is the number of the mesh elements in the x direction.

Overall, the proposed mesh-based MEC model can be applied to the dynamic analysis of the HEMLS, as number, positions, and arrangement of the meshes are designed to remain fixed across different instantaneous motion times. The model's depends on the mesh quantity. The minimum motion step corresponds to the length of the square mesh.

The magnetic flux density component at the central node of element k (Fig.11) can be calculated from the branch flux of the element in the air gap as:

$$B_{kx} = \frac{1}{2} \times \left(\frac{\Phi_{1x}}{S_{yz}} + \frac{\Phi_{2x}}{S_{yz}}\right) \quad (15)$$

$$B_{ky} = \frac{1}{2} \times \left(\frac{\Phi_{1y}}{S_{xz}} + \frac{\Phi_{2y}}{S_{xz}}\right) \quad (16)$$

$$S_{yz} = \pi\left(r_2^2 - r_1^2\right) \quad (17)$$

$$S_{xz} = \pi\left(r_1 + r_2\right)l \quad (18)$$

where r_1 is the inner radius of the element, r_2 is the outer radius of the element.

The static thrust force of the mover of the HEMLS can be obtained as:

$$F_t = \frac{\pi y_r}{\mu_0} \int_0^l B_x(x, y_r) B_y(x, y_r) dx \quad (19)$$

where y_r is the average air-gap radius, l is the axial width of the coupling area between the mover and the rotor at the average air-gap radius y_a. $B_x(x, y_a)$ and $B_y(x, y_a)$ are the axial flux density and radial flux density at y_a.

Due to the interval angle θ in HEMLS, the coupling area between the mover and the rotor's permanent magnet is reduced compared to the traditional MLS, as shown in Fig. 4(c). To address this structural difference, an improved thrust equation based on Equation (5) is proposed for calculating the thrust force of HEMLS, and its expression is as follows:

$$F_t = k_a \times \frac{\pi y_r}{\mu_0} \int_0^l B_x(x, y_r) B_y(x, y_r) dx \quad (20)$$
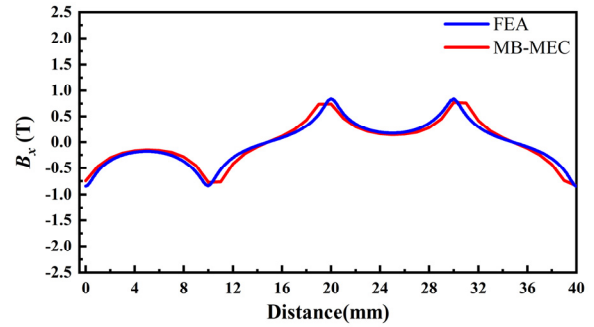
(a)
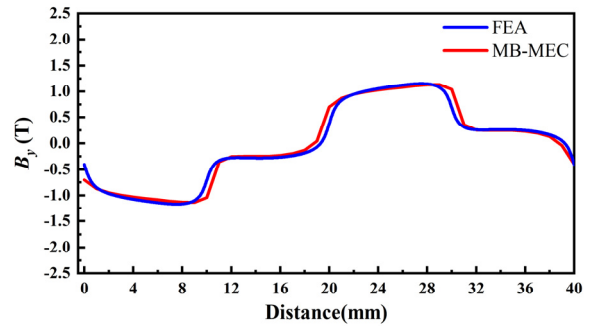
(b)

Fig. 14 The flux density distribution in air gap under load condition ($J = 8$ A/mm^2). (a) B_x. (b) B_y.

> 2024-SECSC-1317 <

where k_a can be expressed as

$$k_a = \frac{\pi - \theta}{\pi} \qquad (21)$$

E. Implementation

The implementation process of the proposed mesh-based MEC model is as follows：

Step. 1: Determine the element number N_{sx} and N_{sy} along the x and y directions, respectively. Then, the length of each mesh l_{mesh} is calculated as l_{sox}/N_{sx} and the height of each mesh, h_{mesh} is equal to l_{soy}/n. And the total number of the elements, n, is given by $N_{sx} \times N_{sy}$. Additionally, the motion step should be the integer multiple of $l_{mesh.}$

Step. 2: Formula the voltage balance equation for an arbitrary mesh k following (7) and (8).

Step. 3: Simultaneous all voltage equations of all meshes to obtain the equations (14) after considering the exciting source and boundary conditions.

Step. 4: Solve (14) using the numerical method outlined in (21) to get the flux of each branch.

Step. 5: Obtain the static thrust force of the mover at the corresponding motion position.

Step. 6: Change the position to the next step and repeat Step. 2 through Step. 5 until all the steps have been calculated.

F. Solution of the equations

Due to the presence of a large reluctance matrix $[R]$ in the proposed mesh based MEC model, the successive over-relaxation method (SOR) is used to solve (14). SOR is an improved Gauss-Seidel iterative method, which is very suitable for solving large matrix equations. Its formulation is as follows:

$$\Phi_i^{(k+1)} = \Phi_i^{(k)} + \frac{\omega}{R_{(i,i)}} \left[-\sum_{j=1}^{i-1} R_{(i,j)} \Phi_j^{(k+1)} - \sum_{j=i}^{n} R_{(i,j)} \Phi_j^{(k+1)} - F_{(i)} \right]$$
$$(22)$$

The convergence condition is expressed as:

$$\left| \Phi_i^{(k+1)} - \Phi_i^{(k)} \right| < \zeta \qquad (23)$$

where ζ is the iterative error and its value is set to 1e-5.

IV. MODEL VALIDATION

To verify the effectiveness and accuracy of the proposed MB-MEC model for HEMLS, it is applied to a HEMLS whose

TABLE II
MATERIALS IN EACH PART OF THE HEMLS

Object	Material
Winding	Copper
PM	NdFe35
Mover	Steel-1008
Rotor	Steel-1008

TABLE III
COMPARISON OF COMPUTATION TIME

Method	FEA	MB-MEC
Time-consuming	5minutes	6 seconds

specification is shown in Table I and Table II. The performance calculation results are then compared between the proposed MB-MEC model and FEA under both no-load and load conditions, respectively.

A. No-load Condition

The comparison results of B in the air gap and the thrust force of the mover between the proposed MB-MEC model and FEA under no-load conditions are presented in Fig. 12 and Fig. 13, respectively. As shown in the figures, the results from both methods align closely. The peak thrust force values obtained from the MB-MEC model and FEA are 0.885 kN and 0.918 kN, respectively, with an error of less than 3.6%.

B. Load Condition

A current density of $J = 8$ A/mm^2 is applied to the exciting winding to verify the effectiveness of the proposed MB-MEC model. The comparison results for B in the air gap and the thrust force of the mover between the proposed MB-MEC model and FEA under load conditions are presented in Fig. 14 and Fig. 15, respectively. As shown in the figures, both methods align closely. The peak thrust force results of the MB-MEC model and FEA are 1.11 kN and 1.17 kN, respectively, with an error of less than 5.1%.

The comparison of peak thrust results between the proposed MB-MEC model and FEA under different values of exciting current is shown in Fig. 16. The figure demonstrates that the peak value of thrust magnitude varies with the exciting current. The peak thrust force calculated by the proposed MB-MEC model is generally consistent with the FEA results, with a maximum error of less than 5.4%, which further validates the accuracy of the proposed MB-MEC model.

The time consumption of the two different methods is compared in Table III. The results indicate that the proposed
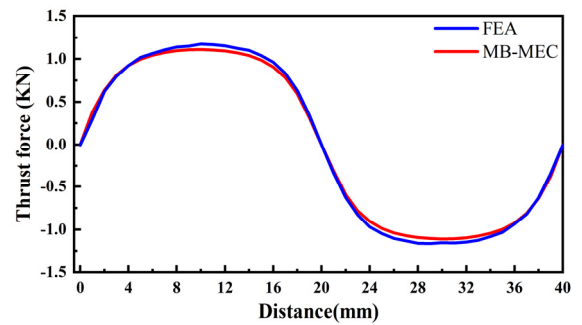

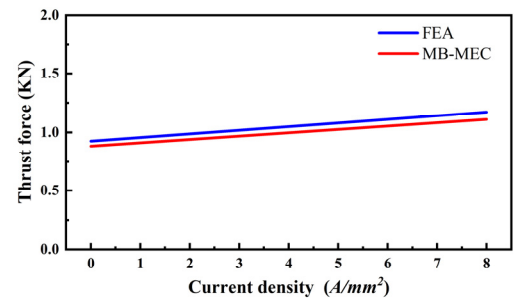**Fig. 15** The comparison results of trust force under load condition ($J = 8$ A/mm^2).

Fig. 16 Comparison results of push-down maximum thrust at different current.
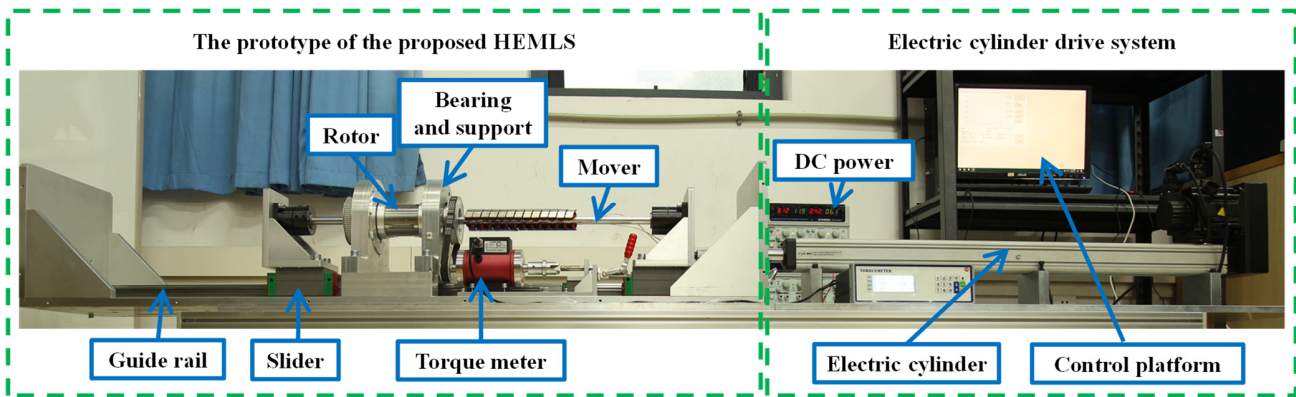
Fig. 17. HEMLS prototype and test platform.

MB-MEC model requires less computation time compared to FEA. Therefore, the MB-MEC model is well-suited for the preliminary design and optimization of the HEMLS, offering a substantial reduction in time consumed in HEMLS design.

V. EXPERIMENT VERIFICATION

To validate the effectiveness of the MB-MEC model, a small experimental prototype of the HEMLS was made and a corresponding test platform was built, as shown in Fig. 17. The main parameters of the small experimental prototype produced are listed in Table IV. An electric cylinder is used to drive the mover of the proposed HEMLS, with the mover and rotor supported by the linear slider and the bearing, respectively.

Each helical PM pole on the inner surface of the rotor consists of 8 segments, forming a circle of spiral magnetic field. As shown in Fig. 18, to ensure accurate installation, the

segmented permanent magnet is mounted using a bolted method with threaded holes drilled on the surface of the segmented permanent magnet and the inner surface of the rotor.

As shown in Fig. 19, the helical teeth are welded to the mover's outer surface, forming a spiral groove between the two spiral teeth. The windings are wound on the spiral tooth, which can generate a helical magnetic field when the current is supplied from a DC power source. Additionally, the spiral permanent magnet blocks are glued to the outer surface of the pole shoes for fixed attachment.

Static torque and thrust force can be measured from the torque meter by driving the mover of the HEMLS with an electric cylinder while the rotor is locked in place. The output thrust force and the position of the electric cylinder are controlled through its controller. When the windings are subjected to current densities of 0 A/mm² and 8 A/mm², the experimental results are compared with the thrust force outcomes of the MB-MEC model, as illustrated in Fig. 20 and

TABLE IV
Main parameters of the prototype

Symbol	Parameters	Values
R_1	Rod radius	10 (mm)
R_2	High moving teeth	22 (mm)
R_3	T tooth outer diameter	25 (mm)
R_4	Actuator outside diameter	27 (mm)
R_5	Inner diameter of rotor	28 (mm)
R_6	Outer diameter of rotor PM	33 (mm)
R_7	Outer diameter of rotor	38.5 (mm)
τ	Rotor PM width	20 (mm)
τ_w	Actuator tooth width	8 (mm)
τ_p	Move PM width	18 (mm)
l	Coupling length	40 (mm)
θ	Interval angle	90°
n_c	Number of windings	45
n_{pm}	Number of turns of rotor PM	1

TABLE V
COMPARISON OF MAXIMUM THRUST FORCE

current density	experiment	MB-MEC	error
$J = 0$ A/mm²	419.59 N	442.73 N	5.2%
$J = 8$ A/mm²	535.2 N	554.6 N	3.6%

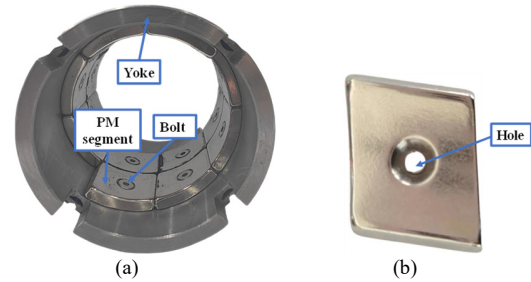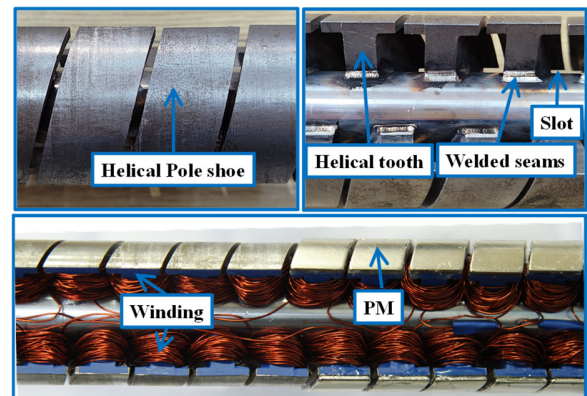**Fig. 18.** (a) the rotor. (b) PM segment.
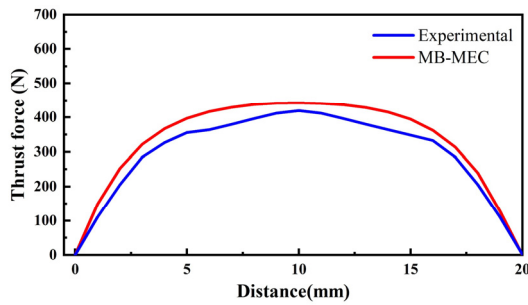

Fig. 19. the mover

Fig. 20. The comparison results of experiment and MB-MEC model under no-load ($J = 0$ A/mm^2) condition.

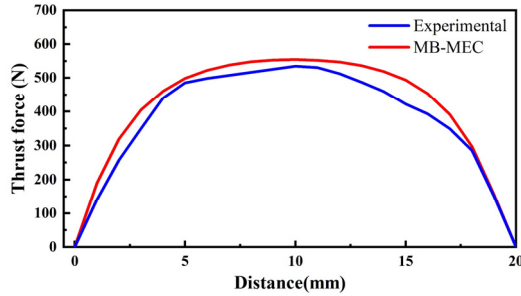**Fig. 21.** The comparison results of the experiment and MB-MEC model under load condition ($J = 8$ A/mm^2).

Fig. 21, respectively. The figures demonstrate good agreement between the experimental and calculation under the different load conditions. Table V compares the maximum thrust from the experimental results and the MB-MEC model under the different. The errors are 5.2% and 3.6%, respectively. The primary source of error is the reduced volume of the PM, caused by drilling in the permanent magnet section of the rotor. As shown in Table V, the maximum thrust when $J = 8$ A/mm^2 is greater than when $J = 0$ A/mm^2. The thrust force of HEMLS can be controlled by adjusting the excitation current of the windings. Consequently, in varying sea states, the maximum thrust can be regulated by the exciting current to enhance the energy conversion efficiency.

VI. CONCLUSION

In this paper, a 2-D MB-MEC model is proposed to analyze the dynamic performance and reduce the time consumption optimization design of the HEMLS. In the proposed MB-MEC model, a universal mesh generation algorithm is proposed to simplify the dynamic motion performance analysis, with each mesh consisting of four basic elements. The basic element considers the magnetic flux of both axial and radial components through the reluctance in different flux path directions. Additionally, both current and PM exciting can be considered at the same time with each basic element. Finally, the proposed MB-MEC model is validated by comparing its results with the static thrust force from the finite element analysis(FEA) and prototype testing under both load and no-load conditions. The results of the proposed MB-MEC align closely with those of FEA and the experiment. Furthermore, the time consumption for a single-period dynamic analysis using the MB-MEC model is only 6 seconds, significantly shorter than that of FEA.

REFERENCES

[1]   J. Ji, Z. Ling, J. Wang, W. Zhao, G. Liu and T. Zeng, "Design and Analysis of a Halbach Magnetized Magnetic Screw for Artificial Heart," in IEEE Transactions on Magnetics, vol. 51, no. 11, pp. 1-4, Nov. 2015, Art no. 8108604.

[2]   N. Berg, R. Holm, and P. Rasmussen, "A novel magnetic lead screw active suspension system for vehicles," in Proc. IEEE Energy Convers. Congr. Expo., Sep. 2014, pp. 3139–3146.

[3]   J. Ji, Z. Ling, J. Wang, W. Zhao, G. Liu, and T. Zeng, "Design and analysis of a Halbach magnetized magnetic screw for artificial heart," IEEE Trans. Magn., vol. 51, no. 11, Nov. 2015, Art. no. 8108604.

[4]   K. Lu and W. Wu, "Electromagnetic lead screw for potential wave energy application," IEEE Trans. Magn., vol. 50, no. 11, Nov. 2014, Art. no. 8205004.

[5]   Holm R K, Berg N I, Walkusch M, et al. Design of a magnetic lead screw for wave energy conversion[J]. IEEE Transactions on Industry Applications, 2013, 49(6): 2699-2708.

[6]   T. Xia, Z. Li, H. Liu, Y. Zhang and H. Yu, "Design of a Magnetic Field Modulated Screw Containing Composite Rotors for Wave Energy Conversion," in IEEE Transactions on Power Electronics, doi: 10.1109/TPEL.2024.3424535.

[7]   S. Meng, Z. Ling, W. Zhao, J. Ji, and M. Xu, "Design and analysis of a surface-inserted magnetic screw with minimum thrust force ripple," IEEE Trans. Transport. Electrific., doi: 10.1109/TTE.2024.3349530.

[8]   L. Zhu, T. Tian, J. Jiang, W. Wu, K. Lu and C. -s. Koh, "A Novel Single-Helix Magnetic Lead Screw for Wave Energy Converter," IECON 2020 The 46th Annual Conference of the IEEE Industrial Electronics Society, Singapore, 2020, pp. 2807-2812.

[9]   L. Zhu, Q. Wu, W. Li, W. Wu, C. S. Koh, and F. Blaabjerg, "A Novel Consequent-Pole Magnetic Lead Screw and Its 3-D Analytical Model with Experimental Verification for Wave Energy Conversion," in IEEE Transactions on Energy Conversion, doi: 10.1109/TEC.2023.3331008.

[10]   Zhu, Lixun, Chao Ma, and Wei Li. 2022. "A Novel Structure of Electromagnetic Lead Screw for Wave Energy Converter," Energies 15, no. 8: 2876.

[11]   K. Lu and W. Wu, "Electromagnetic Lead Screw for Potential Wave Energy Application," in IEEE Trans. Magn., vol. 50, no. 11, pp. 1-4, 2014.

[12]   L. Zhu et al., "A Novel Hybrid Excitation Magnetic Lead Screw and Its Transient Sub-Domain Analytical Model for Wave Energy Conversion," in IEEE Transactions on Energy Conversion, doi: 10.1109/TEC.2024.3354512.

[13]   F. Gao, Q. Wang, J. Zou and Y. Xu, "Development of Equivalent 2-D Finite-Element Models for Accurate Prediction of Thrust Force in Permanent Magnet Lead Screws," in IEEE Transactions on Magnetics, vol. 53, no. 11, pp. 1-4, Nov. 2017.

[14]   L. N. Li, and G. J. Zhu. "Electromagnetic-Thermal-Stress Efforts of Stator-Casing Grease Buffers for Permanent Magnet Driving Motors," IEEE Transactions on Industry Applications, doi: 10.1109/TIA.2023.3291680.

[15]   K. Wang, F. Li, H. Y. Sun, and X. D. Sun, "Consequent Pole Permanent Magnet Machine With Modular Stator," IEEE Trans. Veh. Technol., vol. 69, no. 7, pp. 7054-7063, Jul. 2020.

[16]   X. Sun, Z. Shi, G. Lei, Y. Guo, and J. Zhu, "Multi-objective design optimization of an IPMSM based on multilevel strategy," IEEE Trans. Ind. Electron., vol. 68, no. 1, pp. 139-148, Jan. 2021.

[17]   X. Sun, N. Xu, and M. Yao, "Sequential subspace optimization design of a dual three-phase permanent magnet synchronous hub motor based on NSGA III," IEEE Trans. Transport. Electrific., vol. 9, no. 1, pp. 622-630, Mar. 2023.

[18]   F. Gao, Q. Wang and J. Zou, "Analytical Modeling of 3-D Magnetic Field and Performance in Magnetic Lead Screws Accounting for Magnetization Pattern," in IEEE Transactions on Industrial Electronics, vol. 67, no. 6, pp. 4785-4796, June 2020, doi: 10.1109/TIE.2019.2931241.

[19]   F. Liu, X. Wang and H. Wei, "Fast Magnetic Field Prediction Based on Hybrid Subdomain Method and Multiobjective Optimization Design for Interior Permanent Magnet Synchronous Machines," in IEEE Transactions on Energy Conversion, vol. 38, no. 3, pp. 2045-2060, Sept. 2023, doi: 10.1109.

[20]   Z. Ling, W. Zhao, Y. Sun, J. Ji and M. Xu, "Characteristic Analysis and Harmonic Function Validation of 3-D Modulation Effect for Magnetic

> 2024-SECSC-1317 <

Lead Screw Transmission," in IEEE Transactions on Transportation Electrification, doi: 10.1109/TTE.2024.3399749.

[21] W. Tong, S. Wang, S. Dai, S. Wu and R. Tang, "A Quasi-Three-Dimensional Magnetic Equivalent Circuit Model of a Double-Sided Axial Flux Permanent Magnet Machine Considering Local Saturation," in IEEE Transactions on Energy Conversion, vol. 33, no. 4, pp. 2163-2173, Dec. 2018.

[22] M. Ghods, H. Gorginpour, J. Faiz, M. A. Bazrafshan and M. S. Toulabi, "Design and Enhanced Equivalent Magnetic Network Modeling of a Fractional-Slot Spoke-Array Vernier PM Machine with Rotor Flux Barriers," in IEEE Transactions on Energy Conversion, vol. 38, no. 2, pp. 1060-1072, June 2023.

[23] M. Ghods, J. Faiz, M. A. Bazrafshan, H. Gorginpour and M. S. Toulabi, "Design of an L-Shaped Array Vernier Permanent Magnet Machine for Unmanned Aerial Vehicle Propulsion Using a Schwarz–Christoffel Mapping-Based Equivalent Magnetic Network Model," in IEEE Transactions on Industrial Electronics, vol. 71, no. 1, pp. 237-249, Jan. 2024, doi: 10.1109/TIE.2023.3243307.

[24] H. Saneie and Z. Nasiri-Gheidari, "Performance Analysis of Outer-Rotor Single-Phase Induction Motor Based on Magnetic Equivalent Circuit," in IEEE Transactions on Industrial Electronics, vol. 68, no. 2, pp. 1046-1054, Feb. 2021, doi: 10.1109/TIE.2020.2969125.

[25] A. Baez-Muñoz, F. Trillaud, J. R. Rodriguez-Rodriguez, L. M. Castro and R. Escarela-Perez, "Reluctance-Based Circuit for High-Temperature Superconductor Generator Lumped-Parameter Model," in IEEE Transactions on Magnetics, vol. 58, no. 9, pp. 1-4, Sept. 2022.

[26] X. Li, F. Shen, S. Yu and Z. Xue, "Flux-Regulation Principle and Performance Analysis of a Novel Axial Partitioned Stator Hybrid-Excitation Flux-Switching Machine Using Parallel Magnetic Circuit," in IEEE Transactions on Industrial Electronics, vol. 68, no. 8, pp. 6560-6573, Aug. 2021.

[27] H. Chen and W. Yan, "Flux Characteristics Analysis of a Double-Sided Switched Reluctance Linear Machine Under the Asymmetric Air Gap," in IEEE Transactions on Industrial Electronics, vol. 65, no. 12, pp. 9843-9852, Dec. 2018.

[28] M. Cheng, Z. Xu and G. Zhang, "Vector Magnetic Circuit Based Equivalent Magnetic Network for Flux-Switching Permanent Magnet Machines," in IEEE Transactions on Energy Conversion, doi: 10.1109/TEC.2024.3467949.

[29] P. Naderi, S. Sharouni and M. Heidary, "A Novel Analysis on a New DC-Excited Flux-Switching Machine Using Modified MEC Method for Ground Power Unit Application," in IEEE Transactions on Energy Conversion, vol. 35, no. 4, pp. 1907-1915, Dec. 2020.

[30] G. Watthewaduge and B. Bilgin, "Reluctance Mesh-Based Magnetic Equivalent Circuit Modeling of Switched Reluctance Motors for Static and Dynamic Analysis," in IEEE Transactions on Transportation Electrification, vol. 8, no. 2, pp. 2164-2176, June 2022.

[31] J. Wu, L. Zhu, M. Huang, W. Wu and W. Li, "A Novel Mesh-Based Reluctance Network Model of Hybrid Excitation Magnetic Lead Screw for Wave Energy," 2024 IEEE 7th International Electrical and Energy Conference (CIEEC), Harbin, China, 2024, pp. 3388-3393, doi: 10.1109/CIEEC60922.2024.10583141.

Junfei Wu was born in Zhejiang, China. He is currently working toward the M.S. degree in the department of electrical engineering, Shanghai Maritime University, China.

His research interests include electromagnetic field computation of magnetic lead screws.

Ting Xu was born in Zhejiang, China. He graduated with an M.S. degree in Electrical Engineering from Washington University in St. Louis after earning his bachelor's degree from Shanghai Maritime University, China. His research interests lie in optimization methodologies and computational techniques, including machine learning algorithms to enhance the design and performance of complex engineering systems.

Wei Li (Member, IEEE) was born in Suihua, China. She received her B.S. and M.S. degrees in electrical engineering from Harbin Institute of Technology, Harbin, China, in 2005 and 2007, respectively. She received her Ph. D. degree in electrical engineering from Chungbuk National University, Chungbuk, Korea, in 2011.

She has been an assistant professor at the School of Electronics and Information Engineering at Tongji University, Shanghai, China, since 2012. She is now an associate professor at Tongji University. Her current research interests include hysteresis modeling, finite element method, partial element equivalent method and their applications, control of electrical machines, and so on.

Min Huang (Member, IEEE) received the M.S. degree in electrical engineering from Shanghai Maritime University, Shanghai, China, in 2012, and the Ph.D. degree from the Institute of Energy Technology, Aalborg University, Aalborg, Denmark, in 2015. She is currently a Faculty Member at Shanghai Maritime University. Her research interests include power quality, control, and power converters for renewable energy systems.

Lixun Zhu (Member, IEEE) received his Ph. D. degree in electrical engineering from Chungbuk National University, Korea in 2018. He is an associate professor in the Department of Electrical Engineering at Shanghai Maritime University, China.

His research interests include wave energy conversion, motor design, and iron loss modeling.

> 2024-SECSC-1317 <

Ning Gao (Member, IEEE) was born in Haining, Zhejiang Province, China 1987. He received his B.S. degree in electronics and information engineering from Zhejiang University, Hangzhou, China, in 2009, and his M.S. and Ph.D. degrees from Shanghai Jiao Tong University, Shanghai, China, in 2011 and 2017, respectively. Since 2017, he has been with the Department of Electrical Engineering, Shanghai Maritime University, Shanghai, where he is currently an Assistant Professor. His research interests mainly include control strategies and topologies of power converters applied in battery energy storage systems.

Kangan Wang received the B.S. and Ph.D. degrees in electrical engineering from China University of Mining and Technology, Xuzhou, China, in 2013 and 2019, respectively. Since 2020, he has been with Logistics Engineering College, Shanghai Maritime University. His research interests include power electronic-based smart transformers, cascaded H-bridge converters, and dc-dc converters.

Runhua Fan was born in Yinan, Shandong Province, China 1970. He received his B. S., M. S. and Ph.D. degrees from Shandong University, Jinan, China, in 1991, 1994 and 1998, respectively. Since 2016, he has been a Professor at the College of Ocean Science and Engineering, Shanghai Maritime University, Shanghai, China.

He is mainly interested in metamaterials and their applications in the fields of equipment stealth, electronic components, vibration and noise reduction, hydrophobic anti-icing, etc., and his research on negative dielectric materials has formed a distinctive feature. He has been in charge of the National Natural Science Foundation of China (NSFC), the National Specialized Project, the Shandong Province Achievement Transformation Special Project, and the Shanghai Natural Science Major Project. He has published more than 40 highly cited papers in ESI and has published a monograph, "Negative Dielectric Materials." As a major participant, he organized a series of national conferences on metamaterials and published "Metamaterials Frontier Cross-Science Series".

Chang-Seop Koh (Senior Member, IEEE) received the B.S., M.S., and Ph.D. degrees in electrical engineering from Seoul National University, Seoul, South Korea, in 1982, 1986, and 1992, respectively.

Since 1996, he has been a Professor at the College of Electrical and Computer Engineering, Chungbuk National University, Cheongju, South Korea. His research interests include numerical methods for electromagnetic field analysis, design optimization of electromagnetic devices, and measurement of magnetic properties of silicon steel.

Frede Blaabjerg (Fellow, IEEE) received the Ph.D. degree in electrical engineering from Aalborg University, Copenhagen, Denmark, in 1995, and the Honoris Causa degree from University Politehnica Timisoara, Timisoara, Romania, and Tallinn Technical University, Tallinn, Estonia.

From 1987 to 1988, he was with ABB-Scandia, Randers, Denmark. He became an Assistant Professor in 1992, Associate Professor in 1996, and a Full Professor of Power Electronics and Drives in 1998. Since 2017, he has been a Villum Investigator. He has authored or coauthored more than 600 journal papers in the fields of power electronics and its applications. He is also the coauthor of four monographs and editor of ten books in power electronics and its applications. His current research interests include power electronics and its applications such as in wind turbines, PV systems, reliability, harmonics, and adjustable speed drives.

Dr. Blaabjerg was the recipient of the 32 IEEE Prize Paper Awards, IEEE PELS Distinguished Service Award in 2009, EPE-PEMC Council Award in 2010, IEEE William E. Newell Power Electronics Award 2014, Villum Kann Rasmussen Research Award 2014, Global Energy Prize in 2019 and the 2020 IEEE Edison Medal. He was the Editor-in-Chief of IEEE TRANSACTIONS ON POWER ELECTRONICS from 2006 to 2012.He has been a Distinguished Lecturer for the IEEE Power Electronics Society, from 2005 to 2007, and for the IEEE Industry Applications Society from 2010 to 2011, and 2017 to 2018. During 2019–2020, he was the President of IEEE Power Electronics Society. He is also the Vice-President of the Danish Academy of Technical Sciences Lyngby, Denmark. He is nominated in 2014–2021 by Thomson Reuters to be between the most 250 cited researchers in Engineering in the world.

Dear AE and reviewers,

We sincerely thank you for your valuable comments, which have greatly contributed to improving the quality of our paper. The revised version of the manuscript has been uploaded.

All the modifications are highlighted in **BLUE** within the manuscript. Below, we provide a summary of the changes made in response to your feedback:

<u>**AE:**</u>
Dear Authors,

Thank you for your efforts in improving the paper. However, it is requested you to provide a detailed and satisfactory response to all the comments raised by one of the reviewers.

Check the reviewer comment – " the authors' cursory response to the comments left many questions unanswered". Kindly provide a detailed response to all the comments raised by the reviewer.

<u>Response:</u>
Thank you very much for your kind reminder. In this revised version, we have provided a more detailed response addressing the comments from Reviewer 2. We kindly invite you to review the updated manuscript.

<u>**Reviewer 1:**</u>
Comments to the Author

Good work.
<u>Response:</u>
We sincerely thank you for your valuable feedback and dedicated efforts in helping us improve our manuscript.

<u>**Reviewer 2:**</u>
Comments to the Author

the authors' cursory response to the comments left many questions unanswered.

<u>Response:</u>

We sincerely apologize that our previous response did not fully address the concerns raised by you. Based on your feedback, we have thoroughly revised the paper and included additional results to address the previously overlooked end and saturation effects. We appreciate your time on your rigorous review and kindly invite you to review the revised response below which we hope will provide the necessary clarification.

1) The text is rife with grammatical and spelling errors. There is a need to provide a thorough review.

<u>Response:</u>

We sincerely apologize for the grammatical and spelling errors in the previous version of the manuscript. To address this, we conducted a thorough review and revised the text with the assistance of a bilingual team member to ensure accuracy and clarity. We kindly invite you to review the updated version.

2) The operating principle needs further explanations. Please clarify how a linear movement leads to a rotating speed. Mentioning the details is ineluctable.

<u>Response:</u>

Thank you for your insightful comments. We sincerely apologize for not fully addressing your concerns in our previous response. To clarify, we have further elaborated on the principle of converting linear to rotational motion and have incorporated this explanation into the revised manuscript:

When the poles of the mover and rotor are aligned, as shown in Fig. 2(a), only a radial electromagnetic force (f_r) is generated, which means no torque or thrust is produced. In this configuration, the magnetic screw remains in a stable state. However, when the poles are misaligned, as illustrated in Fig. 2(b), an axial electromagnetic force (f_a) is created from the total magnetic attraction force (F). This axial electromagnetic force leads to rotor torque or mover thrust due to the coupling of the helical-shaped magnetic field in the air gap.

By driving the mover back and forth along the x-axis, this misalignment between the mover and rotor poles results in torque that rotates the rotor. Additionally, the helical magnetic field generated by the mover's windings can be controlled by adjusting the excitation current. For further clarity, a flowchart illustrating the linear-to-rotational motion conversion principle is provided in Fig. 3.

We appreciate your attention to this critical aspect of our work and hope this revised explanation addresses your concerns comprehensively. Thank you again for your feedback.

3) According to the authors, the proposed method ignores the end effect which is an important effect in linear machines. This may decrease the accuracy of the method. How the authors justify the ignorance.

Response:

Thank you for your thoughtful comments. We fully agree with your observation regarding the importance of the end effect in linear machines. To address this, we performed the following analyses:

1. **Air-Gap Magnetic Flux Densities**

   We compared the air-gap magnetic flux densities with and without the end effect. The results, shown in Fig. 1, indicate that the end effect has a limited impact on the overall distribution of the air-gap magnetic field, with noticeable differences only near the end positions.
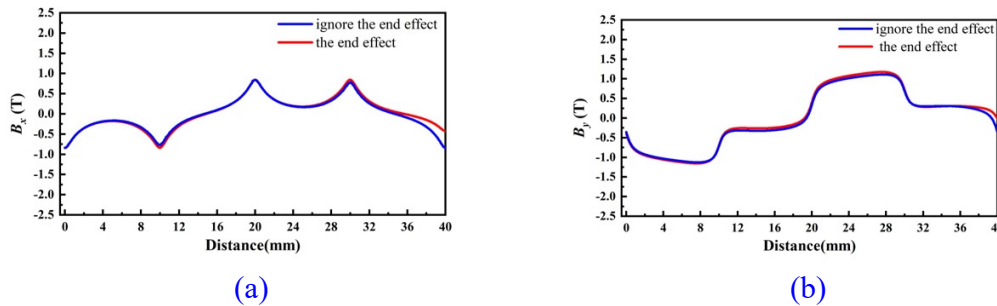

(a)   (b)

Fig. 1 The flux density comparison results with and without the end effect. (a) B_x. (b) B_y.

2. **Comparison of Maximum Thrust**

   We also compared the maximum thrust values with and without considering the end effect, as shown in **Fig. 2**. The results show that accounting for the end effect reduces the maximum thrust by approximately 60 Newtons. Given the relatively small magnitude of this change, we opted to ignore the end effect in the current model.
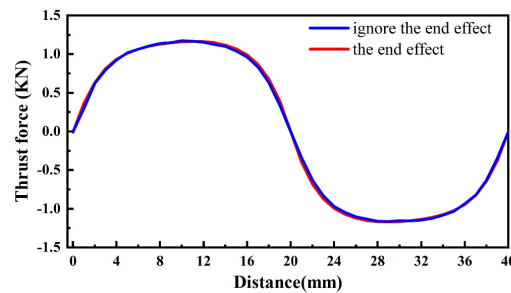

Fig. 2 The thrust force comparison result with and without the end effect.

3. **Dynamic Performance Consideration**

   Since the actuator operates similarly to a mechanical lead screw and its dynamic performance is not critical in this context, analyzing the dynamic torque ripple caused by the end effect is unnecessary. Therefore, we deemed it acceptable to exclude the end effect from our analysis.

Based on the above considerations, we chose to ignore the end effect while developing our model. However, we do acknowledge that including the end effect would more accurately reflect

real-world conditions, thus, in future research, we plan to enhance our model by incorporating the end effect to achieve greater accuracy.

We appreciate your feedback and the opportunity to clarify our approach. Please let us know if further details or analyses are needed.

4) The proposed MEC enjoys some rectangular elements applied to the solution regions. On the other hand, some regions such as air-gap area and PM have a higher level of importance than others. What I'm trying to say is that higher density meshes should be dedicated to these important areas, while lower density meshes may be enough for other regions. This further improves the accuracy of the model while the calculations time remains almost unchanged.

Response:

Thank you very much for your insightful comments. We completely agree with your suggestion.

We sincerely apologize if our previous response did not adequately address your concerns. To clarify, our model does include the functionality to adjust the density of meshes, as you suggested. We regret not making this feature more explicit in our earlier explanation.

To better illustrate this, we have added **Fig. 9** to the revised manuscript, which demonstrates how mesh density is configured in our model to prioritize critical regions such as the air-gap area and permanent magnets (PM). Additionally, for this research, we have already set a sufficient mesh density ($m = 5$) to ensure the required level of calculation accuracy is achieved.

We hope this explanation provides the necessary clarification and addresses your concerns. Please let us know if further details are needed.

5) The proposed method also ignores the saturation effect. This dramatically decreases the accuracy of the proposed solution. Please let me know why the saturation is ignored in the proposed analysis?

Response:

Thank you very much for your valuable comments.

The saturation effect was ignored in our analysis primarily because, under most working conditions, the internal magnetic field distribution does not reach saturation. As a result, excluding the saturation effect allows for a significant reduction in calculation time without compromising accuracy.

To illustrate this, **Fig. 3** shows the magnetic flux distribution in the iron core under no-load and rated load conditions. As demonstrated in the figure, the saturation effect does not occur in the iron core in either scenario:
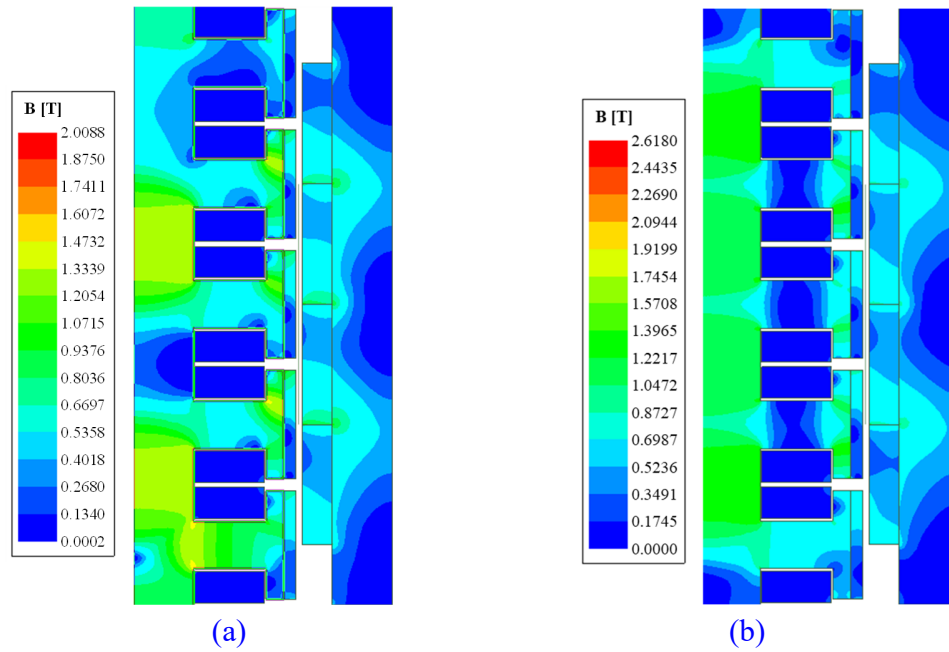
Fig.3 The magnet flux distribution in the iron core. (a) $J = 0\text{A/mm}^2$. (b) $J = 8\text{A/mm}^2$.

Reviewer 3:

Comments to the Author

All the questions have been addressed. Thanks.

Response:

We sincerely appreciate your valuable efforts in helping us improve our manuscript.